



HAL
open science

Magneto-Thermal Metrics Can Mirror the Long-Term Intracellular Fate of Magneto-Plasmonic Nanohybrids and Reveal the Remarkable Shielding Effect of Gold

François Mazuel, Ana Espinosa, Guillaume Radtke, Matthieu Bugnet, Sophie Neveu, Yoann Lalatonne, Gianluigi A. Botton, Ali Abou-Hassan, Claire Wilhelm

► To cite this version:

François Mazuel, Ana Espinosa, Guillaume Radtke, Matthieu Bugnet, Sophie Neveu, et al.. Magneto-Thermal Metrics Can Mirror the Long-Term Intracellular Fate of Magneto-Plasmonic Nanohybrids and Reveal the Remarkable Shielding Effect of Gold. *Advanced Functional Materials*, 2017, 27 (9), pp.1605997. 10.1002/adfm.201605997 . hal-01479779

HAL Id: hal-01479779

<https://hal.sorbonne-universite.fr/hal-01479779>

Submitted on 20 Jul 2018

HAL is a multi-disciplinary open access archive for the deposit and dissemination of scientific research documents, whether they are published or not. The documents may come from teaching and research institutions in France or abroad, or from public or private research centers.

L'archive ouverte pluridisciplinaire **HAL**, est destinée au dépôt et à la diffusion de documents scientifiques de niveau recherche, publiés ou non, émanant des établissements d'enseignement et de recherche français ou étrangers, des laboratoires publics ou privés.

Magneto-Thermal Metrics Can Mirror the Long-Term Intracellular Fate of Magneto-Plasmonic Nanohybrids and Reveal the Remarkable Shielding Effect of Gold

François Mazuel, Ana Espinosa, Guillaume Radtke, Matthieu Bugnet, Sophie Neveu, Yoann Lalatonne, Gianluigi A. Botton, Ali Abou-Hassan, Claire Wilhelm**

Dr. F. Mazuel, Dr. A. Espinosa, Prof. C. Wilhelm

Laboratoire Matière et Systèmes Complexes, UMR 7057, CNRS and University Paris Diderot, 75205 Paris cedex 13, France.

E-mail: claire.wilhelm@univ-paris-diderot.fr

Dr. G. Radtke

Institut de Minéralogie, de Physique des Matériaux et de Cosmochimie (IMPMC), UMR 7590, CNRS, UPMC, 4 place Jussieu, 75005 Paris, France.

Dr. M. Bugnet, Prof. G. A. Botton

Department of Materials Science and Engineering and Canadian Centre for Electron Microscopy, McMaster University, 1280 Main street West, Hamilton, ON, Canada L8S4M1.

Dr. S. Neveu, Dr. A. Abou-Hassan

Sorbonne Universités, Physicochimie des Electrolytes et Nanosystèmes Interfaciaux (PHENIX), UMR 8234, Université Pierre et Marie Curie UPMC-CNRS, 75252 Paris cedex 05, France. E-mail: ali.abou_hassan@upmc.fr

Dr. Y Lalatonne

Inserm, U1148, Laboratory for Vascular Translational Science, UFR SMBH, Université Paris 13, Sorbonne Paris Cité and Service de Médecine Nucléaire, Hôpital Avicenne, Assistance Publique-Hôpitaux de Paris F-93000 Bobigny, France.

Abstract

Multifunctional nanoparticles such as magneto-plasmonic nanohybrids are rising theranostic agents. However, little is yet known of their fate within the cellular environment. In order to reach an understanding of their biotransformations, reliable metrics for tracking and quantification of such materials properties during their intracellular journey are needed. Here, their long-term (one month) intracellular fate was followed within stem-cell spheroids used as tissue replicas. A set of magnetic (magnetization) and thermal (magnetic hyperthermia, photothermia) metrics was implemented to provide reliable insights into the intracellular status. It shows that biodegradation is modulated by the morphology and thickness of the gold shell. First a massive dissolution of the iron oxide core (nanoflower-like) was observed, starting with dissociation of the multi-grain structure. Second, it was demonstrated that an uninterrupted gold shell can preserve the magnetic core and properties (particularly magnetic hyperthermia). In addition to the magnetic and thermal metrics, intracellular high-resolution chemical nanocartography evidenced the gradual degradation of the magnetic cores. Besides, it shows different transformation scenarios, from the release of small gold seeds when the magnetic core is dissolved (interesting for long-term elimination) to the protection of the magnetic core (interesting for long-term therapeutic applicability).

Keywords: biodegradation, magneto-plasmonic nanohybrids, iron oxide nanoflowers, nanomagnetism, magneto-photo-thermia.

1. Introduction

Inorganic nanohybrids have attracted considerable attention in recent years for their multiple functionalities and broad spectrum of activities: Combining distinct components into a single multifunctional hybrid nanostructure can overcome many of the limitations of current therapeutic and diagnostic tools.^[1, 2, 3] Pivotal for the transition from chemistry to nanomedicine, these nanomaterials have been increasingly studied at the nano-bio interface, in biological surroundings, after biochemical interactions, contact with cells, and intracellular sequestration.^[4] However, most studies have focused on short-term functional efficacy and nanoscale immediate modifications, neglecting the long-term (over months) intracellular fate, yet a sensitive issue linked to current nano-safety requirements.^[5]

Among currently developed theranostic nanohybrids, magneto-plasmonic ones are particularly promising, for simultaneous diagnostic and therapeutic applications.^[2, 6, 7, 8] Indeed, each component in the structure brings multiple capabilities: the magnetic entity allows MRI contrast, magnetic targeting and magnetic hyperthermia;^[9] while the plasmonic one allows photothermia, photoacoustic imaging and enhanced optical detection.^[10] Magneto-plasmonic nanohybrids can be prepared using the seed-mediated growth method, their structure and shape being dependent on the properties of each component and on the seed-to-precursor ratio.^[11, 12] Two main architectures currently exist, a symmetrical one composed of a magnetic core (usually iron oxide) and a plasmonic shell (mostly gold),^[6] and a dissymmetrical one such as Janus^[12] and dumbbell-shaped nanostructures.^[3]

The ability to detect and quantify the transformations of nanohybrids inside their target cells over the long-term (at least a month) is essential for all future theranostic applications; yet the study of inorganic nanohybrids biotransformations is still uncharted territory. To date, studies examining the long-term biological fate of inorganic nanomaterials have evaluated usually biodegradation in aqueous media mimicking biological fluids (cell culture media, artificial lysosome-like fluid, serum, plasma)^[13, 14] or directly in vivo after

intravenous injection.^[15] The first scenario allows reliable quantitative measurements but is far removed from the cellular environment, while the second integrates biological complexity but precludes quantitative measurements at the (sub)cellular scale. Recent approaches have pioneered new and sensitive ways of monitoring intracellular nanoparticles integrity status in vitro or in vivo. They are based on labeling nanoparticles core or shell with fluorescent dyes,^[16, 17] radionuclide labels,^[17, 18] or smart molecular rotors ultrasensitive to their microenvironment^[14]. Supplementing this young nanobiodegradation toolbox with methods allowing the tracking of an inorganic core and/or shell in situ, and on the long-term, is still needed.

Many pressing questions thus remain concerning the intracellular fate of inorganic nanohybrids: (i) In a multi-component (e.g. magnetic and plasmonic) system, does each material evolve independently over time? (ii) Does one material influence the fate of the other? For instance, could the inert plasmonic shell protect the highly degradable iron oxide core in the destructive endosomal environment? (iii) Is it possible to selectively monitor magnetic and plasmonic functionalities once a nanohybrid has entered the intracellular medium? and (iv) Will therapeutic functions, such as magneto- and photo-thermal capacity, be undermined by structural biodegradation?

To address all these issues and questions, we used a panel of magneto-plasmonic nanohybrids with tunable gold shells and a 3D tissue-like spheroid model and monitored these nanohybrids over a month following their intracellular incorporation.

We first found that macroscopic magnetic and thermal metrics (at the tissue scale) are direct fingerprints of magneto-plasmonic nanohybrid intracellular integrity, reflecting the extent of nanohybrid multi-component degradation. Second, we observed that the gold shell can reduce or even inhibit intracellular degradation of the iron oxide core, with immediate beneficial impact on long-term serial heating treatments.

2. Results and Discussion

2.1. A Panel of Magneto-Plasmonic Nanohybrids with a Tunable Gold Shell

Magneto-plasmonic nanohybrids (**Figure 1A**) were synthesized with a seed-mediated growth approach as described elsewhere.^[8] In brief, a magnetic iron oxide core (MagNP) was selected to provide high magnetization and efficient magnetic hyperthermia. Produced by thermal decomposition, the core consists of 30 ± 4 nm diameter flower-like (multi-grain) nanoparticles.^[19] Because of their crystalline multi-grain structure, magnetization is maximal (82 emu/g of iron at saturation) and magnetic hyperthermia is very efficient (Specific Absorption Rate (SAR) of about 500 W/g of iron at a magnetic field strength of 18 mT at 470 kHz). The vast accessible surface area allows multiple gold seeds to be grafted. Three magneto-plasmonic hybrids were produced by tuning the ratio of seeds to the available gold salt precursor during the growth step, resulting in the growth of gold of different morphologies (isolated gold nanoparticles, merged) and thicknesses.^[8] The first hybrid, MagPlasNP1 (diameter $d = 39 \pm 4$ nm), consisted of isolated gold nanoparticles (seeds) of 5 to 10 nm attached to the iron oxide core. The second, MagPlasNP2 ($d=47\pm6$ nm), integrated a larger amount of gold, resulting in the formation of voids due to the growth and merging of gold. Finally, with MagPlasNP3 ($d=63\pm11$ nm), the iron oxide surface was almost entirely covered with gold, to a thickness of 33-38 nm. Moreover, based on TEM images, gold coating of the MagPlasNP seems quite uniform and symmetrical for each growth condition which implies that the protective role of the gold layer will be similar for each individual particle and all of the nanoparticles will be dissolved similarly.

2.2. Cellular Internalization of Magneto-Plasmonic Nanohybrids, and Formation of Tissue-Like Spheroids for Long-Term Monitoring

To track the intracellular fate of the magneto-plasmonic nanohybrids, the first step was to allow their cell internalization. Mesenchymal stem cells (MSC) were selected for their ability to organize into tissue-like spheroids, which can be maintained in culture over a period of

months.^[20] No post-incubation cytotoxicity was observed with any of the nanohybrids (Figure S1). Moreover, the iron oxide nanoflower core and all three magneto-plasmonic nanohybrids were easily incorporated by the cells, as demonstrated by single-cell magnetophoresis (Figure S2): after incubation, each cell possessed a magnetic moment due to the magnetic core of the nanohybrid, and migrated towards a magnet. This magnetic migration directly yields the mass of iron incorporated per cell, which was in the range of 1-10 pg. We selected incubation conditions (see Figure S3 and Materials and Methods) to achieve a cellular iron content of about 5 pg for all four nanohybrids. Finally, as shown by transmission electron microscopy (Figure S4), all the nanohybrids were located inside cells, confined within endosomes: none were found attached to the outer membrane or in the extracellular medium.

Cells loaded with nanoparticles and nanohybrids were then assembled into spheroids of 200 000 cells (**Figure 1B**), which were further cultured for a month, with no loss of tissue viability (Figure S5). Note the brown color of the MagNP labeled cellular spheroids, due to the presence of intracellular iron; MagPlasNP1 spheroids become dark brown, with the occurrence of gold seeds, while MagPlasNP2 and MagPlasNP3 spheroids are darker, because the gold shells impose the final color. Note also how the spheroids contract during their maturation (from day 1 to day 25), a change consistent with the formation of a dense tissue-like structure. The tissue-like structure is confirmed by TEM images of the spheroids on day 25 (**Figure 1C**), which show a collagen-rich extracellular matrix surrounding the cells, with the nanomaterials still located intracellularly.

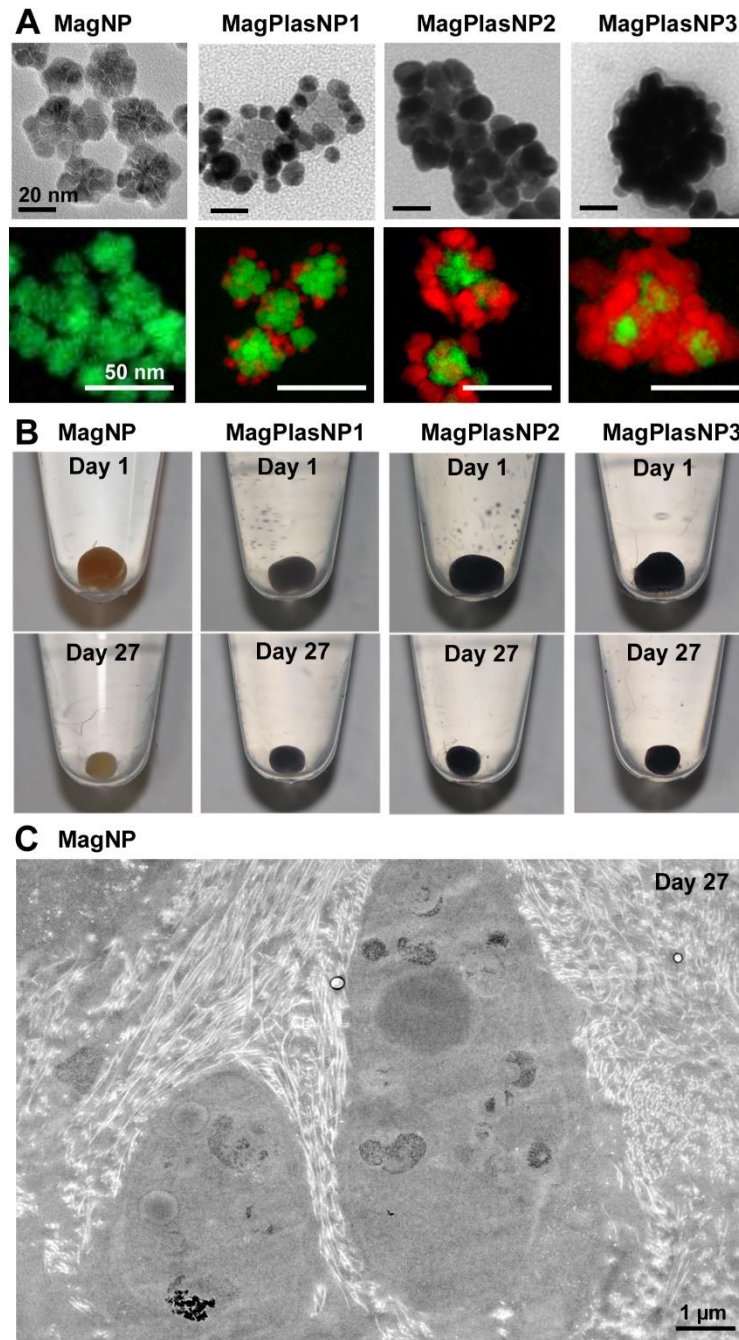


Figure 1: **A.** TEM and STEM-EELS elemental maps of the initial nanohybrid suspensions. Fe maps (green) were obtained using the Fe-L₂₃ edge (~ 708 eV) and Au maps (red) using the Au-M₄₅ edge (~ 2206 eV). MagNP (the iron oxide core of the nanohybrids) is a multi-grain structure, flower-like (also called "nanoflowers"). With the MagPlas nanoparticles, the gold cover grows from 10-nm seeds dispersed on the magnetic core surface (MagPlasNP1), to a connected 33-38-nm shell (MagPlasNP3). **B.** Images of the cellular spheroids on day 1 after their formation, and after 27 days of maturation. Each spheroid contains 200 000 cells, each cell having incorporated nanohybrids prior to spheroid formation (hence the gradual color difference: brown for MagNP containing only iron oxide; becoming increasingly black with

MagPlas as the proportion of gold increases (from MagPlasNP1 to MagPlasNP3). Note that on day 27, the color of MagNP is much less brown, while that of MagPlasNPs is much the same as on day 1, because inert gold doesn't degrade. **C.** TEM image of the inside of a spheroid on day 27, showing cells, still containing nanoparticles (or loaded ferritin), surrounded by a dense collagen matrix (bright filaments), confirming the validity of the cellular spheroids as a model tissue.

2.3. Spheroid Magnetism is a Fingerprint of Intracellular Iron Oxide Magnetic Core Integrity

The first macroscopic parameter linked to the integrity of the iron oxide core within the spheroids is the global magnetization of individual spheroids, which relates directly to the superparamagnetic features provided by the crystalline organization. Magnetization curves and hysteresis loops were recorded at 300 K for single spheroids on day 1 (after spheroid formation) and day 27. **Figure 2A** shows typical hysteresis loops for each nanohybrid at 300K. Cellular spheroid saturation magnetization M_{spheroid} declined markedly from day 1 to day 25 for cells containing MagNP or MagPlasNP1. A smaller decline was noted with MagPlasNP2, while little change was observed with MagPlasNP3. The loss of magnetization provides a direct measure of iron oxide degradation and the degree of degradation (%) can be calculated as $[M_{\text{spheroid}}(\text{day 1}) - M_{\text{spheroid}}(\text{day 27})] / M_{\text{spheroid}}(\text{day 1})$. Averaged over a large number of spheroids ($n > 8$; **Figure 2B**), magnetization declined on average by 70% with MagNP and MagPlasNP1, by 50% with MagPlasNP2 and by only 30% with MagPlasNP3. Of note, the total iron content per spheroid was the same on day 27 as on day 1, as shown by elemental analysis (ICP). The complete magnetic analysis is presented in the supplementary file. In brief, saturation magnetization could be calculated in all cellular conditions (**Table 1**), showing a fall to only 34 emu/g on day 27 with MagNP, but only small decline with MagPlasNP3 (67 emu/g on day 27 vs 86 emu/g on day 1). Fitting of the renormalized magnetization curves with Langevin formalism (Figure S6) yielded a magnetic diameter of 12.8 ± 0.3 nm on day 1 in

all cellular conditions, a value identical to that found in aqueous dispersion. This reflects the multi-grain organization of the 25-nm iron oxide nano-flower, with an effective magnetic size larger than the size of each grain (closer to 9-10 nm in diameter). On day 27, the magnetic size declined with MagNP (10.8 ± 0.3 nm) and MagPlasNP1 (11 ± 0.3 nm), but remained unchanged with MagPlasNP2 and MagPlasNP3. These declines were explained by electron microscopy images (see below), showing dissociation of the multi-grain structure early in the degradation process. Importantly, this decrease does not reflect the dissolution of iron oxide, but only the multi-grain dissociation, and the loss of inter-grains cooperative interactions. Indeed, the massive loss in saturation magnetization recorded for MagNP and MagPlasNP1 simply does not participate to the Langevin analysis of the (renormalized) magnetization curve. The fact that the final magnetic diameter obtained is still in the same range that the one of the single iron oxide grains (11.5 ± 2.5 nm, see next the electron microscopy analysis) reveal that, when started, the iron oxide grains dissolution is rapid, and that intermediate states of partially degraded grains do not impact the magnetic measure. Finally, it is also interesting to note that hysteresis loops were open in cellular conditions at day 0 (enlargements at low magnetic fields are shown in Figure S7), demonstrating interparticle magnetic interactions and/or nanoparticle blocking, but that at day 27, they close in conditions with highest degrees of degradation (especially MagNP), again revealing the dissociation of the iron oxide multi-grain structure.

Table 1. Changes in nanohybrid characteristics, first in the initial suspension, then over time in the cellular environment. Magnetization (emu per gram of total iron) was calculated by renormalizing the magnetic moments at saturation (measured on single spheroids) by the total amount of iron measured by ICP; the magnetic diameter d_{mag} and the polydispersity index σ were retrieved by fitting the magnetization curves with Langevin formalism weighted by the lognormal size distribution (see details in the caption of Figure S6); the specific absorption rate (SAR, in W per gram of total iron) reflects the efficiency of magnetic hyperthermia (at 470 kHz, 18 mT).

		Ms (emu/g)	d_{mag} (nm) / σ	SAR (W/g)
MagNP	initial suspension	89.3±4.5	11.9±0.4 / 0.26±0.04	544±20
	day 1	88.2±14.7	12±0.5 / 0.21±0.04	71.3±3.1
	day 27	34.1±10.6	10.7±0.7 / 0.28±0.06	26.5±8.3
MagPlasNP1	initial suspension	84.3±4.2	12±0.5 / 0.23±0.04	562±11
	day 1	92.7±11.9	11.6±0.5 / 0.25±0.03	143.4±3.3
	day 27	33.4±3.2	10.9±0.5 / 0.26±0.02	50.5±5
MagPlasNP2	initial suspension	86.2±5.4	12.2±0.7 / 0.24±0.04	
	day 1	86.4±12.1	12.1±0.7 / 0.23±0.03	
	day 27	47.4±10.5	11.7±0.8 / 0.25±0.05	
MagPlasNP3	initial suspension	86±4.3	12.3±0.8 / 0.26±0.02	570±10
	day 1	89.8±10.6	12.4±0.9 / 0.25±0.04	144.4±3
	day 27	67.3±8.9	12.2±0.7 / 0.25±0.03	109.4±3.5

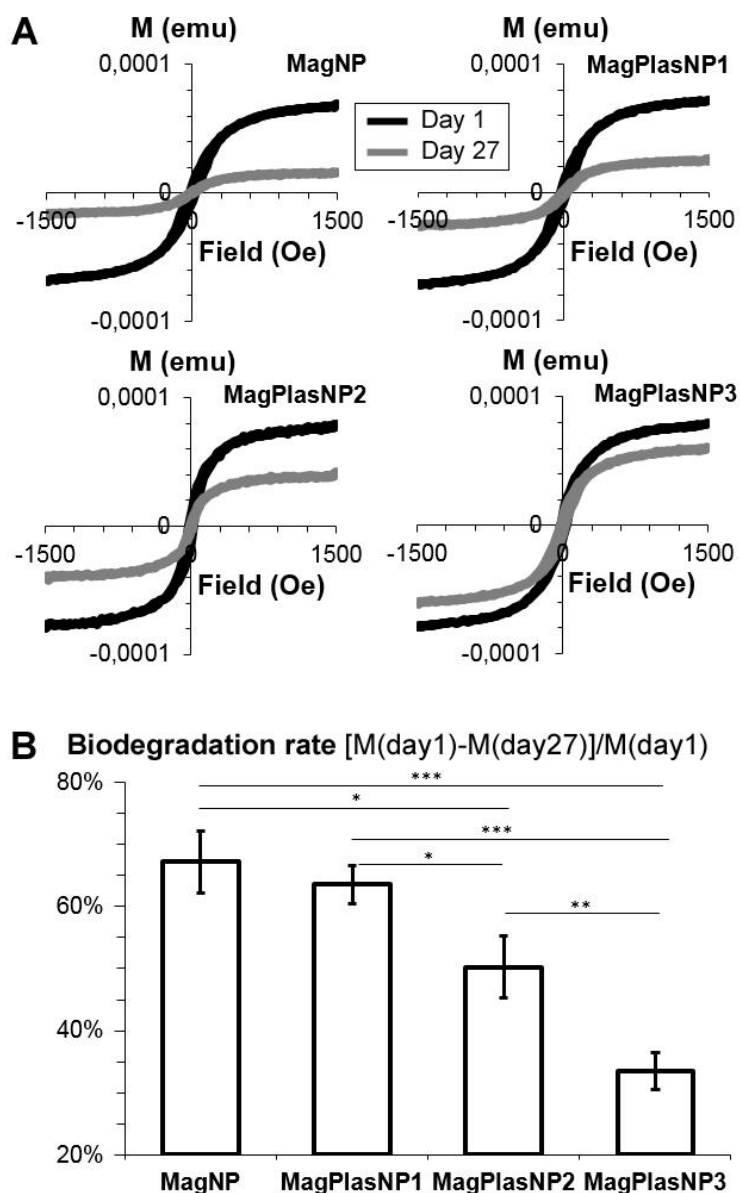


Figure 2: **A.** Typical magnetization curves at 300 K obtained with single spheroids on day 1 and day 27 after spheroid formation. Each cell in a spheroid (200 000 cells) was initially loaded intracellularly with the different nanohybrids (5 pg of iron), namely MagNP and MagPlasNP1, 2 and 3; so that each spheroid should contain on average about 1 μg of iron. This was verified with ICP. Note that the average magnetization on day 1 was of the order of 80 emu/g, matching that found for the initial nanohybrid suspension. By contrast, on day 27, the magnetization declined to 17 emu/g with MagNP; 33 emu/g with MagPlasNP1; 41 emu/g with MagPlasNP2; and only 61 emu/g with MagPlasNP3. All mean values are shown in Table 1. **B.** Degree of biodegradation expressed as the loss of magnetization ($M(\text{day 1})-M(\text{day 27})$) compared to initial magnetization ($M(\text{day 1})$), averaged for multiple spheroids ($n \geq 8$).

2.4. Electron Microscopy Confirms the Shielding Effect of Gold on Iron Oxide Biodegradation

Electron energy-loss spectroscopy (EELS) in the scanning transmission electron microscope (STEM) is widely used for elemental mapping with excellent subnanometric resolution. Although High Angle Annular Dark Field (HAADF) imaging has been occasionally employed to monitor nanobiodegradation,^[21] EELS elemental mapping has never been used in this context, to the best of our knowledge. Here we used a combination of TEM and STEM to follow the intracellular fate of the iron oxide and gold components of the nanohybrids in the spheroid tissue model. **Figure 3** shows the different nanohybrids inside cells, on day 1 and day 27 of tissue maturation. Figures S8 (MagNP), S9 (MagPlasNP1), S10 (MagPlasNP2) and S11 (MagPlasNP3) show additional images. All the nanohybrids were systematically confined within intracellular endosomes, where they remained over the one-month study period. The unmodified shape and content of all the nanohybrids on day 1 show that internalization was not itself detrimental. By contrast, after one month, the picture was clearly different. With MagNP, no intact nanoflowers were detected, while sparse 11 nm-diameter (11.5 ± 2.5 nm in average, distribution shown in Figure S8) iron oxide nanoparticles were still seen within endosomes, coexisting with much more numerous smaller and less dark nanoparticles (5.3 ± 0.9 nm, see Figure S8), identified as ferritin (loaded with free iron), which were present throughout the cytoplasm. The observed dissociation was in perfect agreement with the magnetization curves. With MagPlasNP1 too, abundant ferritin was detected both in endosomes and in the cytoplasm (Figure 3 & Figure S9). Gold seeds were also clearly seen in endosomes but were almost never associated with iron oxide nanoflowers. Some gold seeds (diameter about 10 nm) were isolated, while other were still organized as a shell but with an empty core. Rare intact hybrids were detected. With MagPlasNP2 and MagPlasNP3 (Figure 3 & Figures S10 and S11, respectively), more numerous intact iron oxide cores were observed (especially with MagPlasNP3), with less ferritin accumulation in endosomes and cytoplasm.

Empty gold shells were almost always intact. Taken together, these observations provide a clear picture of iron oxide nanoflower nanodegradation (dissociation of the multi-grain structure, followed by dissolution of single grains and loading of free iron in ferritin), together with the protective role of the gold shell.

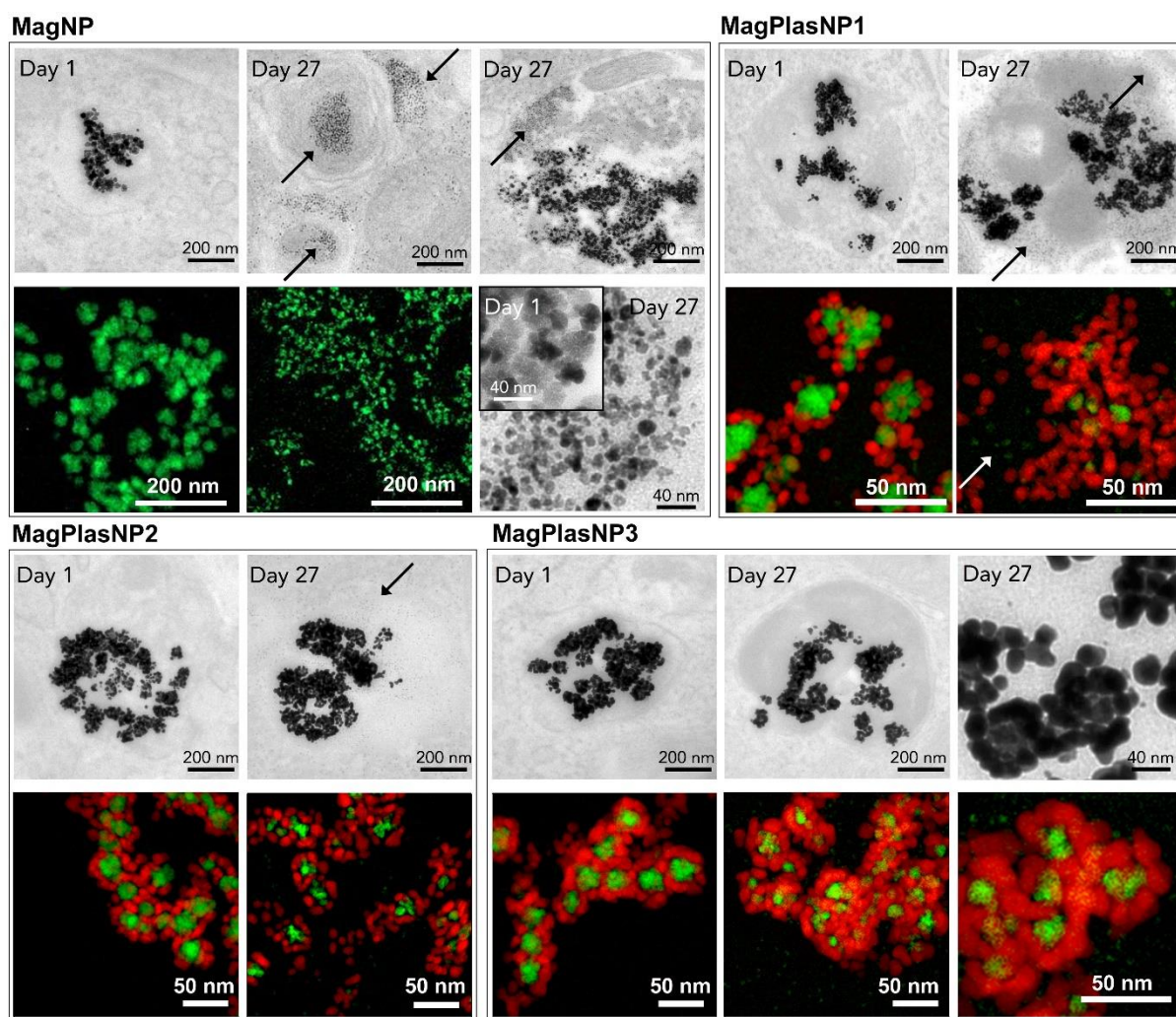


Figure 3: Electron microscopy of nanohybrid shape (TEM) and elemental maps (STEM-EELS, Fe in green, Au in red), on day 1 and day 27. TEM shows that all the nanohybrids were localized intracellularly, within endosomes, on both day 1 and day 27. With MagNP and MagPlasNP1, however, a massive amount of ferritin was observed both in endosomes and in the cytoplasm: for instance, only ferritin is visible in the top center image (MagNP); while ferritin coexists with nanoparticles in endosomes with MagNP and MagPlasNP1 (top right), as indicated by arrows. See also additional images in Figures S8 to 11. Also, with MagNP on day 27, note the clear dissociation of the multi-grain structure into single nanoparticles on STEM (bottom center) and TEM (bottom right, compare with multicore structures on day 1 at

the same magnification) images. With MagPlasNP1, on STEM-EELS maps on day 27 (bottom right), when iron oxide was still present, it appears smaller than the initial multi-grain structure. With MagPlasNP2 and especially MagPlasNP3, intact hybrids are clearly seen on STEM-EELS maps on day 27, as exemplified on the zoom (bottom right) for MagPlasNP3.

2.5. Global Thermal Signatures Capture the Magnetic and Plasmonic Fate of Intracellular Nanohybrids

Intact magneto-plasmonic nanohybrids generate heat when submitted to an alternating magnetic field (magnetic hyperthermia, delivered by the iron oxide core) or to light (photothermia, provided by the plasmonic shell). Their heat-generating capacity might thus reflect the status of intracellular nanohybrids. Magnetic hyperthermia was induced by a magnetic field of 470 kHz and 18 mT, and photothermia with a 680-nm laser at a power of 0.3 W/cm². Both modalities were tested with MagNP, MagPlasNP1 and MagPlasNP3. Heat generation was first characterized in aqueous dispersion. Magnetic hyperthermia efficiency, quantified as the thermal energy production rate per unit mass of iron (SAR, W/g), was similar with the three nanohybrids (Table 1), in the range of 500 W/g, which is very high for the magnetic field setting. By contrast, the photothermic heat elevation (Figure S12) increased gradually from MagNP to MagPlasNP3, in agreement with their respective absorption spectra (also shown in Figure S12). The challenge was then to perform both thermal measurements in cellular conditions. **Figure 4** shows thermal images of cellular spheroid heating on day 1 and day 27 of tissue maturation, together with the average plateau temperature reached (typical temporal heating curves are shown in Figure S13). First, it is noteworthy that the heating measurement was successful in cellular conditions. Second, on the first day after intracellular nanohybrid incorporation (day 1), it is interesting to compare the temperature elevation with that obtained in aqueous dispersion (Figure S12) at the same iron concentration (here corresponding to [Fe]=30 mM). The values were all very similar for photothermia, in aqueous dispersion and in cells, while they were markedly lower for magnetic hyperthermia in cellular

conditions. This was due to the reduction in magnetic relaxation dynamics after cell internalization, secondary to strong confinement within endosomes, as previously demonstrated for a variety of magnetic nanomaterials, including iron oxide nanoflowers. As a result, the specific absorption rate (SAR, Table 1) also fell markedly in cellular conditions (-8-fold for MagNP, -4-fold for MagPlasNPs), with values in the range of 100 W/g (instead of 500 W/g in dispersion). The fact that the SAR fell less markedly with MagPlasNPs is interesting and probably due to a higher interparticle distance inside endosomes (because of the gold shell and polymer coating), which would reduce interparticle interactions that are partly responsible (together with steric hindrance) for the loss of magnetic dynamics.

We now focus on the measurements on day 27. It is first remarkable that the decrease in magnetic hyperthermia perfectly matched the decline in magnetization, reflecting iron oxide degradation. With MagNP, the photo-thermal measurements matched the magnetic measurements, again revealing 70% degradation of the iron oxide nanoflowers. With MagPlasNP1, because the plasmonic shell dominates the heating effect relative to the magnetic core, the loss of less than 15% of photothermal heating matches the 60% degradation of the iron oxide core, suggesting that the gold shell is maintained intact. This was confirmed with MagPlasNP3, in which the gold shell totally dominated photothermal heating: no decrease in heating efficiency was detected on day 27 (also, the iron oxide core was much less degraded).

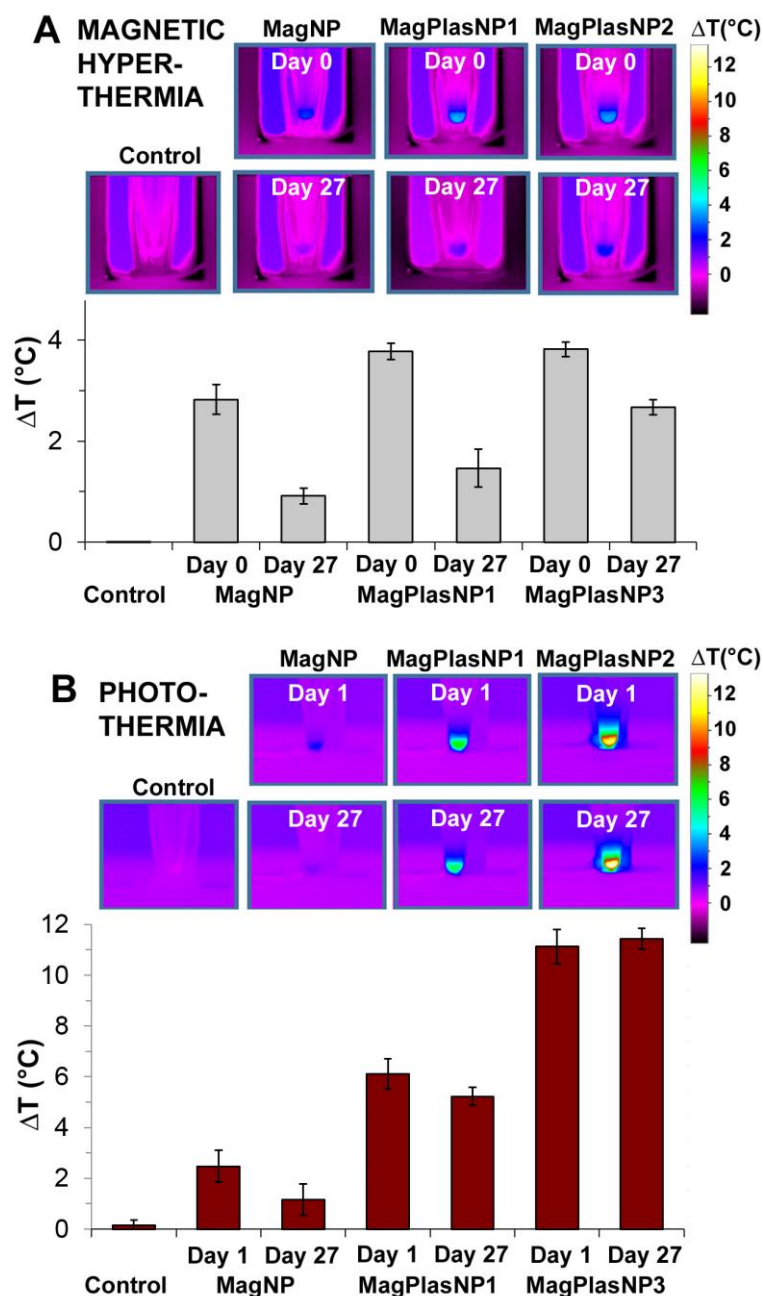


Figure 4: Heat monitoring of magneto-plasmonic nanohybrids within cellular spheroids. Five spheroids were confined within small (0.5 mL) Eppendorf tubes and submitted to magnetic hyperthermia (470 kHz, 18 mT, A) or photothermia (680 nm, 0.3 W/cm², B). Infrared images show the temperature elevation 1 min after the start of magnetic or optical stimulation. The graphs show the average (n≥4) plateau temperature reached in each condition.

2.6. A Set of Metrics to Follow the Nanoscale Multi-Component Intracellular Fate of Nanohybrids

Nanohybrids generally combine different chemical elements to support their multiple functionalities. However, the properties that make nanohybrids so exciting also make it more complex to monitor the long-term intracellular fate of each component, and the interactions between components, once in the biological environment.

Although there are many techniques for characterizing nanomaterials in a dry state or in simple suspension, almost none have been developed to track nanomaterials in a cellular environment over weeks or months. Because of their minute size, nanomaterials pose unique measurement challenges. Electron microscopy is the method of choice to yield nanoscale information on nanomaterials and their environment. However, it is only qualitative and totally destructive, precluding measurements in real time.

Here, we propose magnetic and thermal methodologies for in situ quantitative measurement of parameters that reflect the intracellular behaviour of magneto-plasmonic nanohybrids, in a model tissue maintained in culture for over a month. The idea was to retrieve macroscopic signatures of intracellular nanoparticles that directly reflected their nanoscopic integrity. Thus, the magnetic and thermal approaches provide the same metric reflecting iron oxide core integrity. The fact that magnetic and thermal measurements predict the same degree of iron oxide core degradation is remarkable, because global measurements related to a nano-characteristic, in a biological environment, can produce contrasting results. It is important to note that magnetic measurements not only provide the degree of degradation but also inform on fine structural changes, such as interparticle interactions and dissociation of multi-grain (flower-like) structures into individual grains in the first step of the degradation process. However, these effects only affect the magnetization dynamics (low magnetic field response), while the saturation magnetization must be seen as an absolute indicator of the presence (versus dissolution) of iron oxide structures, in most cases not impacted by dissociation or aggregation of the single grains. Finally, global plasmonic-specific photothermal

measurements were in perfect agreement with qualitative electron microscopy images showing a robust plasmonic gold shell after one month of tissue maturation.

2.7. Impact of Bioprocessing on Therapeutic Potential

Beyond its obvious nanosafety implications, the impact of the cellular environment on nanomaterials also raises concerns as to their therapeutic properties. Medical application of magneto-plasmonic nanohybrids is heat generation through magnetic (hyperthermia) or optic (photothermia) stimulation, together with MRI detection, or magnetic targeting, through magnetic properties. We observed that on the first day of internalization, magnetic properties of all nanohybrids were unchanged. Similarly, photothermia values were identical to those of the initial nanomaterial preparation, indicating that cell internalization did not modify the nanohybrid structure. The magnetic heating potential of all the nanomaterials declined markedly once inside the cells, owing to endosome confinement that impacts their magnetic relaxation but not the structures themselves.

Let us now focus on the situation one month after internalization. Long-term intracellular sequestration was clearly detrimental for the iron oxide core: MagNP were massively degraded (70%), and heating capacity was lost (less than +1°C at best on day 27, for both magnetic hyperthermia and photothermia). This biodegradation of the iron oxide flower-like core was partly or nearly completely prevented by expanding the coverage of the gold shell: with MagPlasNP3 (the most interconnected gold cover), the magnetic core was protected and magnetic hyperthermia was still efficient on day 27 (same efficiency behaviours as with MagNP on day 1). Such gold shell protection of the iron oxide core was expected from the design of the hybrid material, but needed to be demonstrated by in situ measurements within the highly destructive intracellular environment. In return, MagPlasNP3 were efficient for both magnetic hyperthermia and photothermia, even after one month of cellular maturation. This long-term resistance could be extremely useful in tissue engineering applications, for magnetically stimulating an engineered or implanted tissue over long periods for example, or

for MRI monitoring of grafts. Besides, a total protection could be reached by achieving a continuous shell of gold, which could be obtained either by using a higher density of very small gold seeds on the magnetic cores,^[22] or by growing a thin and homogeneous gold shell.^[23] In this second case, an additional growth step will be needed to form anisotropic gold shape with NIR absorption properties.

Between the behaviours observed for MagNP and MagPlasNP3, other interesting situations were evidenced. On day 27, MagPlasNP1 showed degradation of the iron oxide core similar to that seen with MagNP, with multi-grain structure dissociation followed by dissolution. The free iron was loaded into ferritin, which became abundant in endosomes and in the cytoplasm. The gold shell did not degrade, but the 10-nm gold nanoparticles forming the seeds at the surface of the iron oxide were freed as individual nanoparticles. This release of small particles from a larger hybrid structure could represent a strategy to deliver a treatment (such as heat), followed by the elimination of small gold particles by biliary excretion, and iron oxide processing by iron metabolism (e.g. ferritin loading). MagPlasNP2 degradation was also interesting. In this case, the gold shell is cohesive enough to be preserved despite magnetic core degradation, leaving multiple empty gold shells. This demonstrates how the cellular medium can transform nanohybrids into "bio-engineered" structures.

3. Conclusion

We successfully monitored the intracellular fate of magneto-plasmonic nanohybrids within a maturing model tissue, using macroscopic magnetic and thermal metrics as direct signatures of particle integrity. We show that a gold shell coating can prevent the massive intracellular biodegradation of iron oxide nanoflowers and thereby maintain their potential for magnetic hyperthermia, in addition to the excellent photothermal efficiency of the gold shell itself. Besides being the first record of the fate of magneto-plasmonic nanohybrids over a long

period and using spheroids as a model, our results open up new perspectives on the use of cells in nanomaterial synthesis for engineering nanohybrids and assemblies.

4. Experimental Section

Magneto-plasmonic nanohybrids.

Nanohybrids were synthesized using a seed-mediated growth approach previously described.^[8] In brief, citrated iron oxide cores (multi-grain nanoflowers, MagNP) were prepared through a polyol process. The nanoflowers were seeded with gold by reduction of H₂AuCl₄ by NaBH₄ in the presence of ammonia, which resulted in the formation of gold seeds attached to the iron cores. The resulting nanoparticles served as seeds for growing gold of different thicknesses and connectivity (MagPlasNP) by controlling the ratio of gold seeds to gold precursor H₂AuCl₄ in DMF and in presence of PVP as described by Barbosa et al.^[24]

Cell internalization.

Mesenchymal stem cells (MSC, Lonza) were cultured in MSCBM medium (Lonza) at 37°C with 5% CO₂. The cells were grown to passage 4 at 90% confluence before being labeled with the nanohybrids. The labeling was performed in culture medium, at [Fe]=0.1 mM (30 min incubation) for MagNP, [Fe]=0.05 mM for MagPlasNP1 and 2 (overnight incubation), and [Fe]=0.04 mM for MagPlasNP3 (overnight incubation). The different incubation times are due to the different surface coatings (simple citrate absorption for MagNP, PVP coating for MagPlasNP). The polymeric coating slows interactions with cells, thus necessitating longer incubation periods. The iron load per cell was determined at the end of the incubation period by single-cell magnetophoresis. Briefly, cells were detached, resuspended at 0.2 million/mL, introduced into a chamber submitted to a calibrated magnetic gradient (gradB), and video-monitored to track the motion of single labelled cells towards the magnet. Figure S2 shows typical images of magnetic migration. Velocity v_{cell} and radius r_{cell} was then measured by image analysis for 100 independent cells, and converted into a magnetic cellular moment m_{cell} ,

by simply balancing the viscous drag in aqueous medium of water of viscosity η ($6\pi\eta r_{\text{cell}}V_{\text{cell}}$) with the magnetic force ($m_{\text{cell}}\text{grad}B$). m_{cell} can then be converted into a mass of iron by using the saturation magnetization of 80 emu/g. Three independent magnetophoretic measurements were systematically performed, providing the following cellular iron uptake values for the corresponding incubation conditions: $m_{\text{Fe}}(\text{MagNP}) = 5.2 \pm 1.7$ pg; $m_{\text{Fe}}(\text{MagPlasNP1}) = 5.6 \pm 0.9$ pg; $m_{\text{Fe}}(\text{MagPlasNP2}) = 5.8 \pm 1.3$ pg; and $m_{\text{Fe}}(\text{MagPlasNP3}) = 5.7 \pm 1.1$ pg). Of note, to obtain these near-identical values with all four nanohybrids, various incubation conditions were tested (results in Figure S3).

Cellular spheroid formation and maturation.

The tissue maturation medium was composed of high-glucose, serum-free DMEM containing dexamethasone (Sigma, final concentration 0.1 μM), sodium pyruvate (final concentration 1 mM), ascorbic acid-2 phosphate (Sigma, final concentration 50 μM), L-proline (Sigma, 0,35 mM), ITS Premix (BD Biosciences, 1/100 dilution) and TGF- β 3 at 10 ng/mL.

After incubation with the nanohybrids, cells were detached with trypsin and washed with maturation medium. Then 200 000 cells were dispersed in 1 mL of maturation medium in 15-mL centrifuge tubes and spun at 180 g for 2 minutes to form a pellet. The pellets were left in maturation medium at 37°C with 5% CO₂. The medium was changed every 3 days.

On the day of formation (day 1) and after one month of maturation (day 27), the spheroids were collected for magnetic and heating measurements. Measurements can be made on fresh spheroids (on the same day), or after fixation in 10% formalin for one hour before storage in PBS for later measurements. We checked that the fixation process modified neither the magnetic nor the thermal measurements. In particular, the nanoparticle degradation process was stopped by fixation of the aggregate, as confirmed by measuring the magnetization of the same fixed spheroid after two months of storage at 4°C in PBS.

Electron microscopy.

Spheroids were fixed for 1 hour at room temperature with 2.5% glutaraldehyde in 0.1 M cacodylate solution, then for 1 hour at room temperature with 1% OsO₄ in 0.1 M cacodylate solution, before finally being included in Epon resin after dehydration.

For transmission electron microscopy (TEM), ultrathin sections (80 nm) were prepared and deposited on Formvar carbon film 200Mesh copper grids, before being observed with a Phillips Tecnai 12. For scanning transmission electron microscopy (STEM), ultrathin sections (40 nm) were cut, deposited on lacey carbon film 200Mesh copper grids and observed with a FEI Titan Cubed 80-300 operated at 200 kV . Chemical maps were acquired using electron energy-loss spectroscopy (EELS) in STEM mode.

Magnetic measurements.

On day 1 or day 27, spheroids or the initial nanohybrid suspension were introduced into sample capsules for Vibrating Sample Magnetometer analysis (VSM, Quantum Design, Versalab). Field-dependent magnetization curves were measured at 300 K as a function of the external field, in the range 0 to 3 T (step rate of 30 mT/s) to obtain saturation magnetization, and in the range -150 mT to 150 mT, with a step rate of 10 mT/s, for more precise measurements. To convert the magnetic moments thus recorded (in emu) into magnetization (in emu/g), spheroids or suspensions were digested by boiling in a mixture of hydrochloric and nitric acid. Volumes were adjusted to 5 mL with ultrapure water and analyzed with ICP using appropriate iron and gold standards.

Thermal measurements.

In cellular conditions, all measurements were performed in small Eppendorf tubes (0.5 mL) with 5 spheroids (volume 4 μ l), corresponding to an average iron concentration of $[\text{Fe}] = 30 \pm 4$ mM. In aqueous dispersion, measurements were thus systematically done in the same setting, and at the same concentration of $[\text{Fe}] = 30$ mM.

The magnetic hyperthermia applicator (DM3, NanoScale Biomagnetics) is composed of two coils generating a 180-Gauss magnetic field oscillating at 470 kHz. The sample is placed

between the coils and is imaged with an infrared camera (FLIR SC7000) in order to measure the temperature increase. The temperature is measured every second for 2 minutes after magnetic field application at the center of the sample. For magnetic hyperthermia, heating is generally quantified in terms of the specific absorption rate (SAR), the thermal energy production rate per unit mass of iron expressed in W/g. The SAR can be calculated as $SAR = CV/m \cdot dT/dt$, where dT/dt is the initial slope of the heating curve (in °C/s), m is the total mass of iron in the sample, C is the specific heat capacity of the sample ($C_{\text{water}} = 4185 \text{ J/L/K}$; $C_{\text{cells}} = 4125 \text{ J/L/K}$) and V is the sample volume.

For photothermia, each spheroid was illuminated with a 680 nm laser coupled to an optic fiber (Laser Components S.A.S, (France)) at 0.3 W/cm^2 and imaged with an infrared camera (FLIR SC7000) in order to measure the temperature increase. The temperature was measured after 1 minute of illumination.

Supporting Information

Supporting Information is available from the Wiley Online Library or from the author.

Acknowledgements

This work was supported by the European Union (ERC-2014-CoG project MaTissE 648779). Additionally, G.R. acknowledges the Institut de Physique (INP) of Centre National de la Recherche Scientifique (CNRS) for partial financial assistance through a PICS. G. A. B. is grateful to the Natural Sciences and Engineering Research Council (NSERC), Canada, for a Discovery grant partially supporting this work. The STEM and EELS work was carried out at the Canadian Centre for Electron Microscopy, a national facility supported by NSERC, the Canada Foundation for Innovation under the Major Science Initiative program and McMaster University. We also acknowledge for TEM imaging the ImagoSeine core facility of the Institut Jacques Monod, also associated with IBiSA and France BioImaging infrastructures.

References

- [1] L. Zhang, Y. Chen, Z. Li, L. Li, P. Saint-Cricq, C. Li, J. Lin, C. Wang, Z. Su, J. I. Zink, *Angewandte Chemie International Edition* 2016, 55, 2118; W. Liu, B. Naydenov, S. Chakraborty, B. Wunsch, K. Hübner, S. Ritz, H. Cölfen, H. Barth, K. Koynov, H. Qi, *Nano letters* 2016.
- [2] Z.-C. Wu, W.-P. Li, C.-H. Luo, C.-H. Su, C.-S. Yeh, *Advanced Functional Materials* 2015, 25, 6527; C.-H. Wu, J. Cook, S. Emelianov, K. Sokolov, *Advanced Functional Materials* 2014, 24, 6862; G. A. Sotiriou, F. Starsich, A. Dasargyri, M. C. Wurnig, F. Krumeich, A. Boss, J.-C. Leroux, S. E. Pratsinis, *Advanced Functional Materials* 2014, 24, 2818.
- [3] L. Wu, A. Mendoza-Garcia, Q. Li, S. Sun, *Chemical Reviews* 2016, 116, 10473.
- [4] A. E. Nel, L. Mädler, D. Velegol, T. Xia, E. M. Hoek, P. Somasundaran, F. Klaessig, V. Castranova, M. Thompson, *Nature materials* 2009, 8, 543; P. M. Kelly, C. Åberg, E. Polo, A. O'Connell, J. Cookman, J. Fallon, Ž. Krpetić, K. A. Dawson, *Nature nanotechnology* 2015, 10, 472; M. Henriksen-Lacey, S. Carregal-Romero, L. M. Liz-Marzán, *Bioconjugate Chemistry* 2016; E. Mahon, A. Salvati, F. B. Bombelli, I. Lynch, K. A. Dawson, *Journal of Controlled Release* 2012, 161, 164.
- [5] S. J. Soenen, W. J. Parak, J. Rejman, B. Manshian, *Chemical Reviews* 2015, 115, 2109; B. B. Manshian, S. Munck, P. Agostinis, U. Himmelreich, S. J. Soenen, *Scientific reports* 2015, 5; S. J. Soenen, J.-M. Montenegro, A. M. Abdelmonem, B. B. Manshian, S. H. Doak, W. J. Parak, S. C. De Smedt, K. Braeckmans, *Acta biomaterialia* 2014, 10, 732.
- [6] L. Li, S. Fu, C. Chen, X. Wang, C. Fu, S. Wang, W. Guo, X. Yu, X. Zhang, Z. Liu, J. Qiu, H. Liu, *ACS Nano* 2016; J. Huang, M. Guo, H. Ke, C. Zong, B. Ren, G. Liu, H. Shen, Y. Ma, X. Wang, H. Zhang, Z. Deng, H. Chen, Z. Zhang, *Advanced Materials* 2015, 27, 5049; H. Zhou, J.-P. Kim, J. H. Bahng, N. A. Kotov, J. Lee, *Advanced Functional Materials* 2014, 24, 1439.
- [7] H. Wang, G. Cao, Z. Gai, K. Hong, P. Banerjee, S. Zhou, *Nanoscale* 2015, 7, 7885; D. K. Kirui, I. Khalidov, Y. Wang, C. A. Batt, *Nanomedicine: Nanotechnology, Biology and Medicine* 2013, 9, 702; L.-Y. Bai, X.-Q. Yang, J. An, L. Zhang, K. Zhao, M.-Y. Qin, B.-Y. Fang, C. Li, Y. Xuan, X.-S. Zhang, *Nanotechnology* 2015, 26, 315701; Y. Hu, R. Wang, S. Wang, L. Ding, J. Li, Y. Luo, X. Wang, M. Shen, X. Shi, *Scientific reports* 2016, 6.
- [8] A. Espinosa, M. Bugnet, G. Radtke, S. Neveu, G. A. Botton, C. Wilhelm, A. Abou-Hassan, *Nanoscale* 2015, 7, 18872.
- [9] E. Céspedes, J. M. Byrne, N. Farrow, S. Moise, V. S. Coker, M. Bencsik, J. R. Lloyd, N. D. Telling, *Nanoscale* 2014, 6, 12958; D. Soukup, S. Moise, E. Céspedes, J. Dobson, N. D. Telling, *ACS nano* 2015, 9, 231.
- [10] M. Delcea, N. Sternberg, A. M. Yashchenok, R. Georgieva, H. Bäuml, H. Möhwald, A. G. Skirtach, *ACS Nano* 2012, 6, 4169; T. A. Kolesnikova, D. Kohler, A. G. Skirtach, H. Möhwald, *ACS Nano* 2012, 6, 9585; R. Wang, X. Ji, Z. Huang, Y. Xue, D. Wang, W. Yang, *The Journal of Physical Chemistry C* 2015, 120, 377; J. J. Giner-Casares, M. Henriksen-Lacey, M. Coronado-Puchau, L. M. Liz-Marzán, *Materials Today* 2016, 19, 19.
- [11] H. Zeng, S. Sun, *Advanced Functional Materials* 2008, 18, 391; P. Quaresma, I. Osorio, G. Doria, P. A. Carvalho, A. Pereira, J. Langer, J. P. Araujo, I. Pastoriza-Santos, L. M. Liz-Marzán, R. Franco, P. V. Baptista, E. Pereira, *Rsc Adv* 2014, 4, 3659; B. Nikoobakht, M. A. El-Sayed, *Chemistry of Materials* 2003, 15, 1957.
- [12] J. Reguera, D. Jimenez de Aberasturi, N. Winckelmans, J. Langer, S. Bals, L. M. Liz-Marzán, *Faraday Discussions* 2016, 191, 47.
- [13] T. Skotland, P. C. Sontum, I. Oulie, *Journal of pharmaceutical and biomedical analysis* 2002, 28, 323; A. S. Arbab, L. B. Wilson, P. Ashari, E. K. Jordan, B. K. Lewis, J. A. Frank, *NMR in Biomedicine* 2005, 18, 383; L. Gutiérrez, S. Romero, G. B. da Silva, R. Costo, M. D.

- Vargas, C. M. Ronconi, C. J. Serna, S. Veintemillas-Verdaguer, M. del Puerto Morales, *Biomedical Engineering* 2015, 60, 417; A. Ruiz, A. Mancebo, L. Beola, I. Sosa, L. Gutiérrez, *IEEE Magnetics Letters* 2016, 7, 1; Y. Javed, L. Lartigue, P. Hugounenq, Q. L. Vuong, Y. Gossuin, R. Bazzi, C. Wilhelm, C. Ricolleau, F. Gazeau, D. Alloyeau, *Small* 2014, 10, 3325.
- [14] F. Meder, S. S. Thomas, L. W. Fitzpatrick, A. Alahmari, S. Wang, J. G. Beirne, G. Vaz, G. Redmond, K. A. Dawson, *ACS Nano* 2016, 10, 4660.
- [15] R. Mejías, L. Gutiérrez, G. Salas, S. Pérez-Yagüe, T. M. Zotes, F. J. Lázaro, M. P. Morales, D. F. Barber, *Journal of Controlled Release* 2013, 171, 225; B. Freund, U. I. Tromsdorf, O. T. Bruns, M. Heine, A. Giemsa, A. Bartelt, S. C. Salmen, N. Raabe, J. Heeren, H. Itrich, *ACS nano* 2012, 6, 7318; A. Ruiz, L. Gutiérrez, P. Cáceres-Vélez, D. Santos, S. Chaves, M. Fascineli, M. Garcia, R. Azevedo, M. Morales, *Nanoscale* 2015, 7, 16321; N. Feliu, D. Docter, M. Heine, P. del Pino, S. Ashraf, J. Kolosnjaj-Tabi, P. Macchiarini, P. Nielsen, D. Alloyeau, F. Gazeau, R. H. Stauber, W. J. Parak, *Chemical Society Reviews* 2016; A. M. Goodman, Y. Cao, C. Urban, O. Neumann, C. Ayala-Orozco, M. W. Knight, A. Joshi, P. Nordlander, N. J. Halas, *ACS Nano* 2014, 8, 3222.
- [16] J. E. Tengood, I. S. Alferiev, K. Zhang, I. Fishbein, R. J. Levy, M. Chorny, *Proceedings of the National Academy of Sciences* 2014, 111, 4245.
- [17] W. G. Kreyling, A. M. Abdelmonem, Z. Ali, F. Alves, M. Geiser, N. Haberl, R. Hartmann, S. Hirn, D. J. de Aberasturi, K. Kantner, G. Khadem-Saba, J.-M. Montenegro, J. Rejman, T. Rojo, I. Ruiz de Larramendi, R. Ufartes, A. Wenk, W. J. Parak, *Nature nanotechnology* 2015, 10, 619.
- [18] J. Llop, P. Jiang, M. Marradi, V. Gómez-Vallejo, M. Echeverría, S. Yu, M. Puigvila, Z. Baz, B. Szczupak, C. Pérez-Campaña, *Journal of Materials Chemistry B* 2015, 3, 6293.
- [19] L. n. Lartigue, P. Hugounenq, D. Alloyeau, S. P. Clarke, M. Lévy, J.-C. Bacri, R. Bazzi, D. F. Brougham, C. Wilhelm, F. Gazeau, *ACS Nano* 2012, 6, 10935.
- [20] F. Mazuel, A. Espinosa, N. Luciani, M. Reffay, R. Le Borgne, L. Motte, K. Desboeufs, A. Michel, T. Pellegrino, Y. Lalatonne, C. Wilhelm, *ACS Nano* 2016, 10, 7627; F. Mazuel, M. Reffay, V. Du, J.-C. Bacri, J.-P. Rieu, C. Wilhelm, *Physical review letters* 2015, 114, 098105.
- [21] J. D. López-Castro, A. V. Maraloiu, J. Delgado, J. Calvino, M.-G. Blanchin, N. Gálvez, J. M. Domínguez-Vera, *Nanoscale* 2011, 3, 4597.
- [22] Z. ur Rahman, Y. Ma, J. Hu, Y. Xu, W. Wang, X. Chen, *Rsc Adv* 2014, 4, 5012; C. S. Levin, C. Hofmann, T. A. Ali, A. T. Kelly, E. Morosan, P. Nordlander, K. H. Whitmire, N. J. Halas, *ACS Nano* 2009, 3, 1379.
- [23] M. Abdulla-Al-Mamun, Y. Kusumoto, T. Zannat, Y. Horie, H. Manaka, *Rsc Adv* 2013, 3, 7816; S. M. Silva, R. Tavallaie, L. Sandiford, R. D. Tilley, J. J. Gooding, *Chemical Communications* 2016, 52, 7528.
- [24] S. Barbosa, A. Agrawal, L. Rodríguez-Lorenzo, I. Pastoriza-Santos, R. A. Alvarez-Puebla, A. Kornowski, H. Weller, L. M. Liz-Marzán, *Langmuir* 2010, 26, 14943.

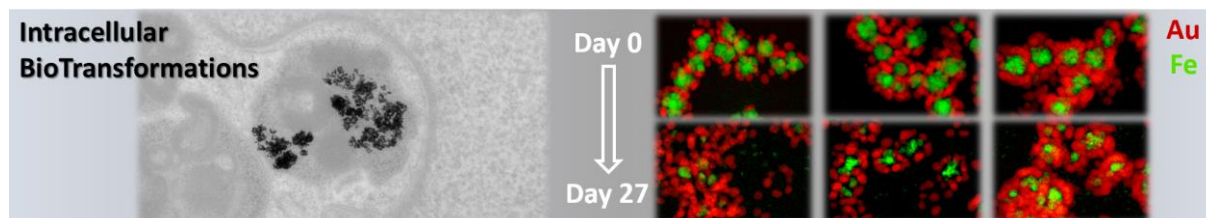
Table of contents entry

The structural and functional changes of magneto-plasmonic nanohybrids in the local intracellular environment is investigated. It is found that (i) magnetic and thermal metrics can act as macroscopic quantitative fingerprints of the intracellular fate of hybrid magneto-plasmonic nanomaterials, and that (ii) the measured massive biodegradation of the magnetic core can be prevented by fine-tuning the inert gold shell.

Keyword nanomagnetism, magneto-photo-thermia, magneto-plasmonic nanohybrids, iron oxide nanoflowers, intracellular biodegradation

F. Mazuel, A. Espinosa, G. Radtke, M. Bugnet, S. Neveu, Y. Lalatonne, G. A. Botton, A. Abou-Hassan*, C. Wilhelm*

Magneto-Thermal Metrics Can Mirror the Long-Term Intracellular Fate of Magneto-Plasmonic Nanohybrids, and Reveal the Remarkable Shielding Effect of Gold



ToC figure (110 mm broad × 20 mm high).